

CONFIRMATION OF WIDE-FIELD SIGNATURES IN REDSHIFTED 21 CM POWER SPECTRA USING MURCHISON WIDEFIELD ARRAY OBSERVATIONS

NITHYANANDAN THYAGARAJAN^{1*}, DANIEL C. JACOBS¹, JUDD D. BOWMAN¹, N. BARRY², A. P. BEARDSLEY²,
 G. BERNARDI^{3,4,5}, F. BRIGGS^{6,7}, R. J. CAPPALLO⁸, P. CARROLL², A. A. DESHPANDE⁹, A. DE OLIVEIRA-COSTA¹⁰,
 JOSHUA S. DILLON¹⁰, A. EWALL-WICE¹⁰, L. FENG¹⁰, L. J. GREENHILL⁵, B. J. HAZELTON², L. HERNQUIST⁵, J. N. HEWITT¹⁰,
 N. HURLEY-WALKER¹¹, M. JOHNSTON-HOLLITT¹², D. L. KAPLAN¹³, HAN-SEEK KIM^{14,7}, P. KITTIWISIT¹, E. LENC^{15,7},
 J. LINE^{14,7}, A. LOEB⁵, C. J. LONSDALE⁸, B. MCKINLEY^{14,7}, S. R. MCWHIRTER⁸, D. A. MITCHELL^{16,7}, M. F. MORALES²,
 E. MORGAN¹⁰, A. R. NEBEN¹⁰, D. OBEROI¹⁷, A. R. OFFRINGA^{6,7}, S. M. ORD^{11,7}, SOURABH PAUL⁹, B. PINDOR^{14,7},
 J. C. POBER², T. PRABU⁹, P. PROCOPIO^{14,7}, J. RIDING^{14,7}, N. UDAYA SHANKAR⁹, SHIV K. SETHI⁹, K. S. SRIVANI⁹,
 R. SUBRAHMANYAN^{9,7}, I. S. SULLIVAN², M. TEGMARK¹⁰, S. J. TINGAY^{11,7}, C. M. TROTT^{11,7}, R. B. WAYTH^{11,7},
 R. L. WEBSTER^{14,7}, A. WILLIAMS¹¹, C. L. WILLIAMS¹⁰, J. S. B. WYTHE^{14,7}

Draft version May 20, 2015

ABSTRACT

Here we confirm a recently predicted and previously unknown foreground signature in the 3D power spectra of high-redshift 21 cm measurements, wherein the interferometer is sensitive to large-scale structure on all baselines. This is due to the inherently chromatic nature of a wide-field instrument response and is characterized by enhanced power from foreground emission in Fourier modes adjacent to those considered to be most sensitive to the cosmological H I signal. Thus it is a critical input to design and analysis choices of future instruments such as the Hydrogen Epoch of Reionization Array and the Square Kilometre Array. The simulation in our recent paper which predicted this feature was validated against Murchison Widefield Array data but this key element was at or below the noise level. In this paper, we improve the Murchison Widefield Array data sensitivity through coherent averaging of 12 independent snapshots aligned in local sidereal time across different observing nights, and provide the first confirmation of the prediction with a signal-noise ratio > 10 .

Subject headings: cosmology: observations — dark ages, reionization, first stars — large-scale structure of universe — methods: statistical — radio continuum: galaxies — techniques: interferometric

1. INTRODUCTION

The epoch of reionization (EoR) commenced following the formation of the first stars and galaxies. It is characterized by a period of non-linear growth of matter density perturbations and astrophysical evolution in the Universe's history. Detection of redshifted 21 cm radiation of H I from this epoch is one of the most promising probes of the evolution of large scale structure during this epoch (Sunyaev & Zeldovich 1972; Scott & Rees 1990; Madau et al. 1997; Tozzi et al. 2000; Iliev et al. 2002).

Sensitive instruments such as the Square Kilometre Array (SKA) with the capability of direct imaging of redshifted H I are yet to become operational. In the meanwhile, the Hydrogen Epoch of Reionization Array¹⁹ (HERA), currently under development, will be much more advanced in its capability to detect and place definitive constraints on the reionization epoch relative to current instruments such as the Murchison Widefield Array (MWA; Lonsdale et al. 2009; Tingay et al. 2013; Bowman et al. 2013), the Low Frequency Array (LOFAR; van Haarlem et al. 2013), and the Precision Array for Probing the Epoch of Reionization (PAPER; Parsons et al. 2010), which have only enough sensitivity for a statistical detection of the signal (Bowman et al. 2006; Parsons et al. 2012a; Beardsley et al. 2013; Dillon et al. 2013; Thyagarajan et al. 2013; Pober et al. 2014).

The primary challenge to detection of cosmological H I from the EoR arises from continuum emission from Galactic and extragalactic foreground objects, which

¹ Arizona State University, School of Earth and Space Exploration, Tempe, AZ 85287, USA

² University of Washington, Department of Physics, Seattle, WA 98195, USA

³ Square Kilometre Array South Africa (SKA SA), Park Road, Pinelands 7405, South Africa

⁴ Department of Physics and Electronics, Rhodes University, Grahamstown 6140, South Africa

⁵ Harvard-Smithsonian Center for Astrophysics, Cambridge, MA 02138, USA

⁶ Australian National University, Research School of Astronomy and Astrophysics, Canberra, ACT 2611, Australia

⁷ ARC Centre of Excellence for All-sky Astrophysics (CAASTRO)

⁸ MIT Haystack Observatory, Westford, MA 01886, USA

⁹ Raman Research Institute, Bangalore 560080, India

¹⁰ MIT Kavli Institute for Astrophysics and Space Research, Cambridge, MA 02139, USA

¹¹ International Centre for Radio Astronomy Research, Curtin University, Perth, WA 6845, Australia

¹² Victoria University of Wellington, School of Chemical & Physical Sciences, Wellington 6140, New Zealand

¹³ University of Wisconsin–Milwaukee, Department of Physics, Milwaukee, WI 53201, USA

¹⁴ The University of Melbourne, School of Physics, Parkville, VIC 3010, Australia

¹⁵ The University of Sydney, Sydney Institute for Astronomy, School of Physics, NSW 2006, Australia

¹⁶ CSIRO Astronomy and Space Science (CASS), PO Box 76, Epping, NSW 1710, Australia

¹⁷ National Centre for Radio Astrophysics, Tata Institute for Fundamental Research, Pune 411007, India

* e-mail: t_nithyanandan@asu.edu

¹⁹ <http://reionization.org/>

is $\sim 10^4$ stronger than the desired signal. However, the inherent differences in spatial isotropy and spectral smoothness can be exploited to extract the cosmological signal from foreground contamination (see, e.g., Di Matteo et al. 2002, 2004; Zaldarriaga et al. 2004; Furlanetto & Briggs 2004; Morales & Hewitt 2004; Santos et al. 2005; Furlanetto et al. 2006; McQuinn et al. 2006; Morales et al. 2006; Wang et al. 2006; Gleser et al. 2008). Thus, a detailed characterization of foreground emission has become essential (Ali et al. 2008; Bowman et al. 2009; Liu et al. 2009; Bernardi et al. 2009, 2010; Datta et al. 2010; Liu & Tegmark 2011; Ghosh et al. 2012; Morales et al. 2012; Parsons et al. 2012b; Trott et al. 2012; Pober et al. 2013; Dillon et al. 2013; Dillon et al. 2014; Liu et al. 2014a,b; Thyagarajan et al. 2013, 2015).

Our recent study (Thyagarajan et al. 2015, hereafter referred to as Paper I) used all-sky foreground and instrument models for the first time in order to simulate actual EoR experiments more accurately than previous studies. Surprisingly, we found that foreground emission outside the primary beam field of view caused the most significant contamination of Fourier modes considered most sensitive for detecting the cosmological H I signal in delay spectrum based analyses. This contamination is the result of the interplay between foreground emission, particularly diffuse Galactic emission, and the wide-field properties typical of EoR instruments. Our simulations predicted that delay spectra from the MWA and other experiments should exhibit a characteristic “pitchfork” appearance with local maxima near the horizon delay limits, in addition to at the primary lobe region.

A careful design of antenna aperture can significantly mitigate this contamination. Optimal weighting of foreground-contaminated Fourier modes may be required to extract the signal with maximum sensitivity. Thus, knowledge of such detailed foreground signatures is key for design and analysis choices of future instruments such as HERA and SKA.

In Paper I, we verified the general features of our simulations against MWA observations, but were unable to confirm the *pitchfork* prediction due to insufficient sensitivity in the small amount of data analyzed. Here, we use deeper MWA data to confirm with high significance the presence of key *pitchfork* characteristics of wide-field measurements predicted in the preceding study.

§2 is an overview of the role of wide-field measurements in the delay spectral domain and the predicted *pitchfork* signature. §3 describes the analysis of MWA data used to improve the dynamic range of the delay spectra. §4 describes the results and confirms the presence of the predicted wide-field effects. §5 underscores their impact on aperture design. §6 summarizes our findings.

2. WIDE-FIELD EFFECTS IN DELAY SPECTRUM

Paper I describes in detail the effects of wide-field measurements as seen in the delay spectra of interferometer *visibilities*. We list the relevant equations and give a brief overview of the wide-field signatures predicted therein.

The delay spectrum for a baseline vector, \mathbf{b} , is (Parsons et al. 2012a,b; Thyagarajan et al. 2013, Paper I):

$$\tilde{V}_b(\tau) \equiv \int V_b(f) W(f) e^{i2\pi f\tau} df, \quad (1)$$

with interferometer visibilities, $V_b(f)$, given by (van Cittert 1934; Zernike 1938; Thompson et al. 2001):

tert 1934; Zernike 1938; Thompson et al. 2001):

$$V_b(f) = \iint_{\text{sky}} A(\hat{\mathbf{s}}, f) I(\hat{\mathbf{s}}, f) W_i(f) e^{-i2\pi f \frac{\mathbf{b} \cdot \hat{\mathbf{s}}}{c}} d\Omega \quad (2)$$

$$= \iint_{\text{sky}} \frac{A(\hat{\mathbf{s}}, f) I(\hat{\mathbf{s}}, f)}{\sqrt{1 - l^2 - m^2}} W_i(f) e^{-i2\pi f \frac{\mathbf{b} \cdot \hat{\mathbf{s}}}{c}} dl dm, \quad (3)$$

where, $I(\hat{\mathbf{s}}, f)$ and $A(\hat{\mathbf{s}}, f)$ are the sky brightness and antenna’s directional power pattern, respectively, as a function of frequency (f) and direction on the sky denoted by the unit vector $\hat{\mathbf{s}} \equiv (l, m, n)$, $W_i(f)$ denotes instrumental bandpass weights, $W(f)$ is a spectral weighting function that controls the transfer function in the delay transform, $d\Omega = (1 - l^2 - m^2)^{-1/2} dl dm$ is the solid angle element to which $\hat{\mathbf{s}}$ is the unit normal vector, and c is the speed of light. $\tau = \mathbf{b} \cdot \hat{\mathbf{s}}/c$ is the geometric delay between antenna pairs measured relative to the zenith and provides a mapping to position on the sky.

The delay power spectrum is defined as (Parsons et al. 2012a, Paper I):

$$P_d(\mathbf{k}_\perp, k_\parallel) \equiv |\tilde{V}_b(\tau)|^2 \left(\frac{A_e}{\lambda^2 \Delta B} \right) \left(\frac{D^2 \Delta D}{\Delta B} \right) \left(\frac{\lambda^2}{2k_B} \right)^2, \quad (4)$$

with

$$\mathbf{k}_\perp \equiv \frac{2\pi(\frac{\mathbf{b}}{\lambda})}{D}, \quad (5)$$

$$k_\parallel \equiv \frac{2\pi\tau f_{21} H_0 E(z)}{c(1+z)^2}, \quad (6)$$

where, A_e is the effective area of the antenna, ΔB is the bandwidth, λ is the wavelength of the band center, k_B is the Boltzmann constant, f_{21} is the rest frequency of the 21 cm radiation of H I, z is the redshift, $D \equiv D(z)$ is the transverse comoving distance, ΔD is the comoving depth along the line of sight, and h , H_0 and $E(z) \equiv [\Omega_M(1+z)^3 + \Omega_K(1+z)^2 + \Omega_\Lambda]^{1/2}$ are standard cosmology terms. In this paper, we use $\Omega_M = 0.27$, $\Omega_\Lambda = 0.73$, $\Omega_K = 1 - \Omega_M - \Omega_\Lambda$, and $H_0 = 100 \text{ km s}^{-1} \text{ Mpc}^{-1}$. $P_d(\mathbf{k}_\perp, k_\parallel)$ is in units of $\text{K}^2(\text{Mpc}/h)^3$.

The defining characteristics of the *pitchfork* signature are understood as follows. The steep rise in subtended solid angle near the horizon for a fixed delay bin size significantly enhances the integrated emission near the horizon delay limits in wide-field measurements. This is found to be true for diffuse emission even on wide antenna spacings because their foreshortening towards the horizon makes them sensitive to large angular scales that match the inverse of their foreshortened lengths. We confirm this key feature using deeper MWA data.

3. MWA OBSERVATIONS

The MWA instrument configuration, EoR observing strategy, and analysis procedure applied to individual snapshots used in this study are already described in Paper I and references therein. *Off-zenith* data containing the Galactic center in Paper I was useful in demonstrating the mapping between delay spectra and sky locations, establishing primary causes of foreground contamination,

and devising a technique for mitigating foreground contamination. *Pitchfork* signatures which result from low-level ubiquitous diffuse emission are fainter. Since Galactic plane emission, even from directions far away from the primary field of view, can potentially swamp the fainter *pitchfork* signatures, zenith pointings which have a maximum avoidance of the Galactic plane are preferred for this study.

To reduce thermal fluctuations while maintaining coherence, it is essential to average independent data sets obtained over the same region of sky with identical instrument settings. Hence, we select a subset of MWA snapshots each of duration 112 seconds obtained over different nights which are aligned to within 72 seconds of each other in *local sidereal time* (LST) around a mean LST of 0.04 hours with the MWA tile beam pointed at zenith. The database contains 14 snapshots satisfying these criteria. Two of these snapshots, which contained amplitude and phase artifacts for a significant duration across different baselines, are excluded from our analysis. Results of this coherent averaging are discussed below.

4. RESULTS

Figure 1 shows the delay spectra obtained from a single snapshot of MWA data (top), averaging LST aligned delay spectra from 12 individual snapshots from MWA observations on different nights (middle), and from modeling with no thermal noise fluctuations shown for reference (bottom). In all panels, the *foreground wedge* bounded by horizon limits (white dotted lines) is prominent. The bright horizontal branch of power at $\tau \simeq 0$ corresponds to foreground emission from the main lobe of the antenna power pattern pointed at the zenith.

In the single snapshot (top), similar to the one used in our earlier study, faint features associated with the *pitchfork* signature are visible near the horizon limits. But the high level of thermal fluctuations makes their significance marginal. In contrast, the dynamic range in the averaged data (middle) is a factor $\gtrsim 10$ higher (in delay power spectrum) relative to that in a single snapshot, and is consistent with the improvement expected from averaging 12 independent snapshots. Hence, the foreground power near the horizon limits appears $\gtrsim 10$ times more prominent. Also, faint horizontal features, not seen in the single snapshot, appear at $\tau \simeq \pm 0.78 \mu\text{s}$ thus confirming the improvement in sensitivity. We identify these faint features as the response of the MWA coarse band edges flagged periodically every 1.28 MHz.

In these observations, the Galactic center is just about to set in the west. Its signature on eastward baselines is seen in the modeled delay spectra (bottom panel) as a marginal brightening of the arm near the negative horizon limit for $|\mathbf{b}| < 125$ m, consistent with our findings in Paper I. This spills over into higher delay modes resulting in the faint ($\lesssim 10^2 \text{ K}^2 (\text{Mpc}/h)^3$) vertical stripes at $|\mathbf{b}| < 50$ m. The corresponding vertical feature is identified in the averaged data as well.

In order to show that low-level ubiquitous diffuse emission is a significant contributor to the *pitchfork* signature, contribution from any strong emission from near the Galactic center needs to be minimized. This is best illustrated with northward antenna spacings which map any residual emission from this region to $\tau \simeq 0$ and thus reduce the impact on higher delay modes (Paper I). Fig-

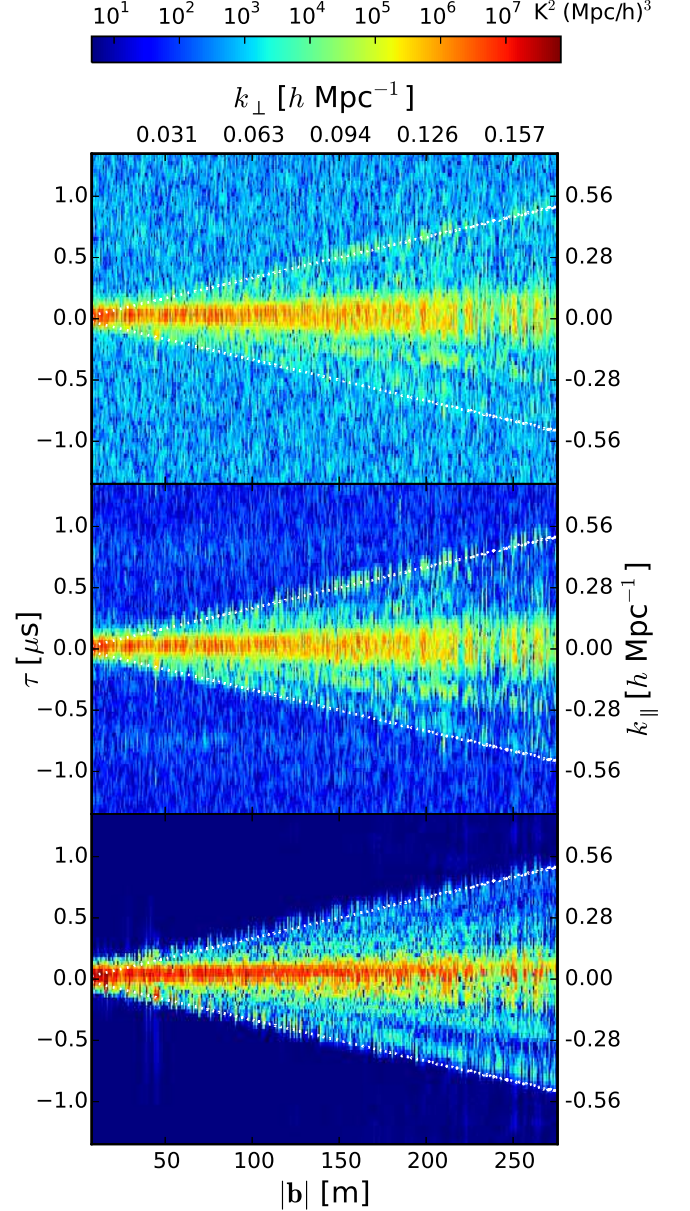


FIG. 1.— Delay power spectra obtained from a single snapshot (top), by averaging 12 snapshots of LST aligned MWA data (middle), and from modeling with no thermal noise added (bottom). The x -axis, denoted by $|\mathbf{b}|$ (and k_{\perp}), represents angular (and spatial) scales in the plane of the sky while the y -axis, shown in τ and k_{\parallel} , denotes the spatial scales along the line of sight. White dotted lines are the horizon delay limits. Dynamic range in the delay power spectra of MWA data has increased by a factor ~ 10 after averaging (middle) relative to that in a single snapshot (top). Power near the horizon limits caused by wide-field effects are prominent. Faint horizontal features at $\tau \simeq \pm 0.78 \mu\text{s}$ are visible due to effective lowering of thermal fluctuations and are the response to periodic coarse band edge flagging of MWA data every 1.28 MHz.

ure 2 shows the averaged delay power spectra on three selected baseline vectors oriented northward. Data and noiseless models are shown in black and red respectively. The horizontal dotted black line denotes rms of thermal fluctuations estimated from data. The vertical dashed

line denotes horizon delay limits, and the vertical dotted-dashed lines denote delays at which the responses to coarse band edge flagging are expected.

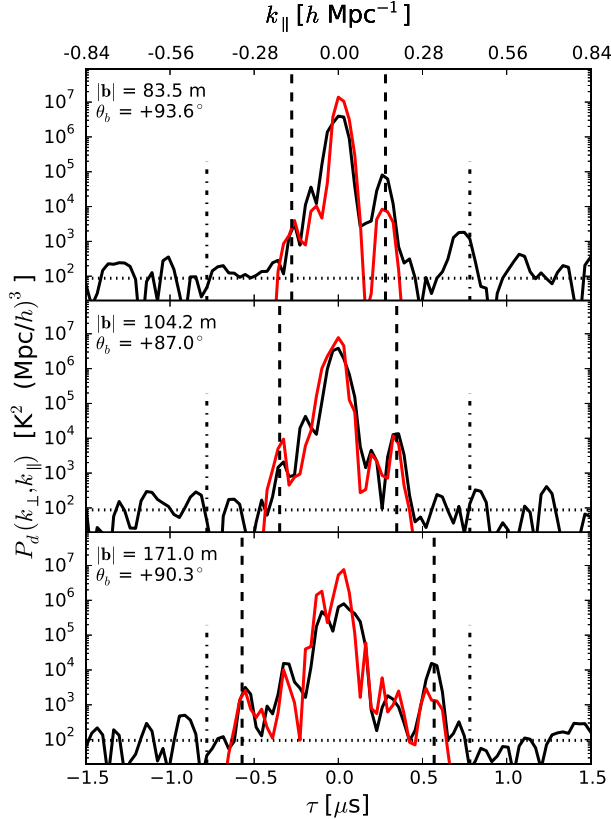


FIG. 2.— Delay power spectra on three antenna spacings oriented northward, obtained by coherent averaging of 12 snapshots aligned in LST. The averaged data and models are shown in black and red respectively. The antenna spacings are 83.5 m (*top*), 104.2 m (*middle*), and 171 m (*bottom*). The horizontal dotted line is the *rms* of thermal fluctuations. The vertical dashed lines denote the horizon delay limits. The vertical dotted-dashed lines at $\tau = \pm 0.78 \mu\text{s}$ correspond to grating responses of periodic flagging of bandpass at intervals of 1.28 MHz. The peaks close to the horizon delay limits are distinctly visible at $\sim 10\text{-}1000 \sigma$ levels. Differences between model and data are primarily attributed to uncertainties in the foreground model and the MWA tile power pattern.

We focus on the prominent peaks in data near the horizon limits. Typically, the power near the negative horizon limit is seen with a signal-noise ratio $\sim 10\text{-}100$, while that around the positive horizon limit is $\sim 100\text{-}1000$.

There is a remarkable agreement in broad morphology between the data and the model. However, some differences in the amplitude scales are noted. For instance, the emission near the positive horizon limit is higher in the data than in the model in both figures. We attribute such differences to uncertainties in the foreground model, the MWA tile power pattern, thermal fluctuations, and other uncertainties noted in Paper I which limit a more thorough quantitative comparison between the model and the data. In fact, this lays further emphasis on the need for extending the footprint of surveys matching the frequency and angular resolution of observation such as the MWA Commissioning Survey (MWACS; Hurley-Walker et al. 2014) and the Galactic and Extragalactic MWA

Survey (GLEAM; Wayth et al. submitted) to cover the entire hemisphere, and a detailed characterization of the power pattern over the entire hemisphere.

We note that reducing uncertainties will only change the relative strength of the *pitchfork* signature in our model. However, the effects giving rise to this signature are generic to all wide-field measurements. Thus, the extremely high significance detection of foreground emission near the horizon limits is a robust confirmation of the predicted wide-field measurement phenomenon.

5. IMPACT ON INSTRUMENT DESIGN

Delay spectrum maps the geometric delays to positions of foreground objects on the sky. Thus the directional power pattern of the antenna has a direct impact on the delay spectrum. Since the contamination in the *EoR window* is strongly dependent on sources of emission close to the horizon, design of antenna apertures that suppress their sensitivity towards the horizon is important.

We approached this issue in Paper I via simulations of different antenna apertures, namely, a dipole, a phased array, and a dish. The relative foreground contamination in the *EoR window* was found to be roughly $10^4 : 10^2 : 1$ respectively. In addition, the foreground contamination inside the *foreground wedge* was found to be suppressed by a factor 10^4 for a dish relative to an MWA-like phased array thus raising the possibility of accessing the EoR signal in *k*-modes inside the *foreground wedge*.

The response of new instruments such as SKA and HERA to foreground contamination has to be investigated thoroughly. With the SKA at low frequencies, plans to deploy “stations” of ~ 35 m diameter that act as aperture arrays consisting of 256 pseudo-randomly placed vertical log-periodic dipole antennas are being considered. The “station beam” will be obtained by a phased addition of the dipole responses. The typical horizon response of these beams is $\gtrsim 30$ dB lower than at zenith²⁰ but the randomness across different stations in the placement of dipoles is expected to reduce the response significantly further as pairs of station voltage beams are multiplied with each other. HERA will use dishes that limit response near the horizon to $\lesssim -40$ dB, ~ 20 dB lower than that of the MWA. Their precise beam responses and the resulting foreground contamination, especially near the horizon, will prove to be critical and timely inputs to their aperture designs which are in their final stages.

6. SUMMARY

Using deeper MWA data, we have confirmed with high significance the earlier prediction that wide-field EoR measurements suffer significant foreground contamination from near the horizon. This has important implications for instrument design and data analysis of future instruments such as HERA and SKA. Precise modeling is thus required to gain a complete understanding of the characteristics of the cosmological signal and the foregrounds.

In our earlier study, we proposed a selective flagging of data on different baselines that can potentially mitigate foreground contamination by two orders of magnitude. Following the confirmation presented here, efforts

²⁰ SKA memo “Station Response and Imaging Performance of LFAA: 100 MHz to 600 MHz” by Razavi-Ghods et al.

are underway to incorporate this proposed foreground mitigation technique into the MWA data analysis.

For future work, we plan to extend our analysis to HERA. It is a closely packed hexagonal array of fixed 14 m dishes which will observe the sky drifting overhead with redundant antenna spacings. Based on our earlier study, such a dish will have a much desirable Fourier response from a foreground contamination viewpoint. One of our objectives is to forecast the per-baseline foreground contamination as a function of local sidereal time in order to tune the HERA observing strategy and data analysis to maximize sensitivity to the EoR signal.

This work was supported by the U. S. National Science Foundation (NSF) through award AST-1109257. DCJ is supported by an NSF Astronomy and Astrophysics Postdoctoral Fellowship under award AST-1401708. JCP is supported by an NSF Astronomy and Astrophysics Fellowship under award AST-1302774. This work makes use of the Murchison Radio-astronomy Observatory, operated by CSIRO. We acknowledge the Wajarri Yamatji people as the traditional owners of the Observatory site. Support for the MWA comes from the NSF (awards: AST-0457585, PHY-0835713, CAREER-0847753, and AST-0908884), the Australian Research Council (LIEF

grants LE0775621 and LE0882938), the U.S. Air Force Office of Scientific Research (grant FA9550-0510247), and the Centre for All-sky Astrophysics (an Australian Research Council Centre of Excellence funded by grant CE110001020). Support is also provided by the Smithsonian Astrophysical Observatory, the MIT School of Science, the Raman Research Institute, the Australian National University, and the Victoria University of Wellington (via grant MED-E1799 from the New Zealand Ministry of Economic Development and an IBM Shared University Research Grant). The Australian Federal government provides additional support via the Commonwealth Scientific and Industrial Research Organisation (CSIRO), National Collaborative Research Infrastructure Strategy, Education Investment Fund, and the Australia India Strategic Research Fund, and Astronomy Australia Limited, under contract to Curtin University. We acknowledge the iVEC Petabyte Data Store, the Initiative in Innovative Computing and the CUDA Center for Excellence sponsored by NVIDIA at Harvard University, and the International Centre for Radio Astronomy Research (ICRAR), a Joint Venture of Curtin University and The University of Western Australia, funded by the Western Australian State government.

REFERENCES

- Ali, S. S., Bharadwaj, S., & Chengalur, J. N. 2008, *MNRAS*, 385, 2166
- Beardsley, A. P., Hazelton, B. J., Morales, M. F., et al. 2013, *MNRAS*, 429, L5
- Bernardi, G., de Bruyn, A. G., Brentjens, M. A., et al. 2009, *A&A*, 500, 965
- Bernardi, G., de Bruyn, A. G., Harker, G., et al. 2010, *A&A*, 522, A67
- Bowman, J. D., Morales, M. F., & Hewitt, J. N. 2006, *ApJ*, 638, 20
- . 2009, *ApJ*, 695, 183
- Bowman, J. D., Cairns, I., Kaplan, D. L., et al. 2013, *PASA*, 30, 31
- Datta, A., Bowman, J. D., & Carilli, C. L. 2010, *ApJ*, 724, 526
- Di Matteo, T., Ciardi, B., & Miniati, F. 2004, *MNRAS*, 355, 1053
- Di Matteo, T., Perna, R., Abel, T., & Rees, M. J. 2002, *ApJ*, 564, 576
- Dillon, J. S., Liu, A., & Tegmark, M. 2013, *Phys. Rev. D*, 87, 043005
- Dillon, J. S., Liu, A., Williams, C. L., et al. 2014, *Phys. Rev. D*, 89, 023002
- Furlanetto, S. R., & Briggs, F. H. 2004, *New A Rev.*, 48, 1039
- Furlanetto, S. R., Oh, S. P., & Briggs, F. H. 2006, *Phys. Rep.*, 433, 181
- Ghosh, A., Prasad, J., Bharadwaj, S., Ali, S. S., & Chengalur, J. N. 2012, *MNRAS*, 426, 3295
- Gleser, L., Nusser, A., & Benson, A. J. 2008, *MNRAS*, 391, 383
- Hurley-Walker, N., Morgan, J., Wayth, R. B., et al. 2014, *PASA*, 31, 45
- Iliev, I. T., Shapiro, P. R., Ferrara, A., & Martel, H. 2002, *ApJ*, 572, L123
- Liu, A., Parsons, A. R., & Trott, C. M. 2014a, *Phys. Rev. D*, 90, 023018
- . 2014b, *Phys. Rev. D*, 90, 023019
- Liu, A., & Tegmark, M. 2011, *Phys. Rev. D*, 83, 103006
- Liu, A., Tegmark, M., Bowman, J., Hewitt, J., & Zaldarriaga, M. 2009, *MNRAS*, 398, 401
- Lonsdale, C. J., Cappallo, R. J., Morales, M. F., et al. 2009, *IEEE Proceedings*, 97, 1497
- Madau, P., Meiksin, A., & Rees, M. J. 1997, *ApJ*, 475, 429
- McQuinn, M., Zahn, O., Zaldarriaga, M., Hernquist, L., & Furlanetto, S. R. 2006, *ApJ*, 653, 815
- Morales, M. F., Bowman, J. D., & Hewitt, J. N. 2006, *ApJ*, 648, 767
- Morales, M. F., Hazelton, B., Sullivan, I., & Beardsley, A. 2012, *ApJ*, 752, 137
- Morales, M. F., & Hewitt, J. 2004, *ApJ*, 615, 7
- Parsons, A., Pober, J., McQuinn, M., Jacobs, D., & Aguirre, J. 2012a, *ApJ*, 753, 81
- Parsons, A. R., Pober, J. C., Aguirre, J. E., et al. 2012b, *ApJ*, 756, 165
- Parsons, A. R., Backer, D. C., Foster, G. S., et al. 2010, *AJ*, 139, 1468
- Pober, J. C., Parsons, A. R., Aguirre, J. E., et al. 2013, *ApJ*, 768, L36
- Pober, J. C., Liu, A., Dillon, J. S., et al. 2014, *ApJ*, 782, 66
- Santos, M. G., Cooray, A., & Knox, L. 2005, *ApJ*, 625, 575
- Scott, D., & Rees, M. J. 1990, *MNRAS*, 247, 510
- Sunyaev, R. A., & Zeldovich, Y. B. 1972, *A&A*, 20, 189
- Thompson, A. R., Moran, J. M., & Swenson, Jr., G. W. 2001, *Interferometry and Synthesis in Radio Astronomy*, 2nd Edition (Wiley)
- Thyagarajan, N., Udaya Shankar, N., Subrahmanyan, R., et al. 2013, *ApJ*, 776, 6
- Thyagarajan, N., Jacobs, D. C., Bowman, J. D., et al. 2015, *ApJ*, 804, 14
- Tingay, S. J., Goeke, R., Bowman, J. D., et al. 2013, *PASA*, 30, 7
- Tozzi, P., Madau, P., Meiksin, A., & Rees, M. J. 2000, *ApJ*, 528, 597
- Trott, C. M., Wayth, R. B., & Tingay, S. J. 2012, *ApJ*, 757, 101
- van Cittert, P. H. 1934, *Physica*, 1, 201
- van Haarlem, M. P., Wise, M. W., Gunst, A. W., et al. 2013, *A&A*, 556, A2
- Wang, X., Tegmark, M., Santos, M. G., & Knox, L. 2006, *ApJ*, 650, 529
- Zaldarriaga, M., Furlanetto, S. R., & Hernquist, L. 2004, *ApJ*, 608, 622
- Zernike, F. 1938, *Physica*, 5, 785